

USING TAGGED MRI TO RECONSTRUCT A 3D HEARTBEAT

Magnetic resonance imaging tissue tagging is a decade-old method that lets scientist follow the motion of a beating heart. The method described here reconstructs 3D motion from multiple 2D MRI images to find new information about the right ventricle

In the past two decades, researchers have determined that the human heart's right ventricle—the chamber that receives blood from the right atrium and from which blood is forced out into the pulmonary artery—plays an important role in normal and abnormal hemodynamics.¹ Moreover, because the RV shares a wall with the left ventricle called the septum (see “The right ventricle” sidebar), diseases that affect the RV can also affect the LV and lead to heart failure. Some diseases can alter the normal motion and deformation of the RV's free wall and the septum, and because the RV pumps blood into the pulmonary system, lung abnormalities can also adversely affect it. A method that could quantify abnormal RV kinematics might help detect the presence and severity of such diseases.

To detect abnormal motion, we must first characterize the kinematics of a normal RV. However, the RV's complex geometry and motion patterns have made it difficult to analyze. Early studies used implanted radiopaque markers, which provided limited knowledge about RV

motion, primarily in animals.² Recently, imaging modalities such as echocardiography, computed tomography, and conventional magnetic resonance imaging (MRI) have provided a non-invasive means for studying the RV,² but using these techniques to observe and measure wall motion is difficult due to the RV wall's lack of landmarks, its relative thinness, and its complex geometry.

Although MRI tissue-tagging techniques provide a noninvasive way to study the RV's wall motion in humans,³ 2D images cannot capture deformation and motion across the image's plane. So far, researchers have been only able to reconstruct the 3D motion from multiple views primarily of the LV,⁴ and there's been just one preliminary study of the RV's mid-wall.⁵ Therefore, our goal is to recover the full 3D motion of the RV walls from information in tagged MRI images. However, when developing a 3D motion reconstruction technique from tagged MRI, the RV's anatomy poses several challenging problems:

- With current MRI resolution, a limited number of tags fall on the RV wall.
- We can't describe RV geometry using any simple primitive.
- RV wall motion varies temporally and regionally, making it difficult to describe concisely.

The right ventricle

The human heart's right ventricle receives deoxygenated blood from the right atrium and pumps it into the pulmonary artery and out to the lungs (see Figure A). It appears crescentlike in a cross-sectional view, and, unlike the left ventricle, it is difficult to approximate with any simple parameterized 3D shape. The RV shares a common wall (the septum) with the LV, while its free outer wall is in mechanical contact with the pericardium (the membranous sac surrounding the heart) and, through it, the lungs. We can conceptually separate the RV cavity into a rough-walled inflow tract and a relatively smooth outflow tract.¹ The normally 3- to 5-mm-thick RV free wall is thin relative to the LV's 9- to 11-mm-thick free wall.¹

Reference

1. J.W. Hurst, *Atlas of the Heart*, Gower Medical, New York, 1988.

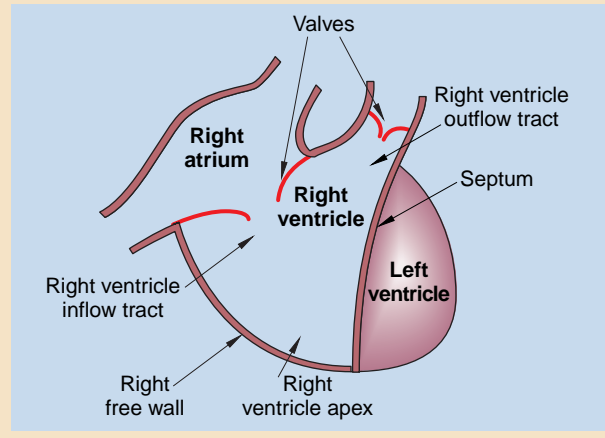


Figure A. A partial schematic of the heart's anatomy. The right ventricle lies to the front (toward the chest wall) and to the right of the left ventricle. The RV and LV share a wall called the septum.

- The RV exhibits significant motion (> 10 mm) through both short- and long-axis image planes.

We present a new methodology that overcomes these problems and effectively captures RV shape and motion using tagged MRI data.

3D models

To perform an accurate model-based 3D motion reconstruction, we need a detailed description of the RV's geometry. Because the septum plays such an important role in the function of both ventricles, our approach is to create a biventricular geometric model. We defined the geometry first by generating a volumetric finite-element mesh based on contour information from the images. This mesh is the starting point for recovering the 3D motion from the MRI images. In computer vision terminology, this mesh is the deformable model that is fit to data extracted from the images.

Each reconstructed 3D model provides a dense and detailed set of motion data; the methodology's final phase is to translate this data into both global and local motion variables. We use principal strains and directions as indicators of contraction, because they are independent of any coordinate system. Computer graphics techniques can help visualize the motion quantities in 3D.

Our 3D motion reconstruction technique is the center of several interrelated techniques. Figure 1 shows a flowchart of these techniques and the flow of information between them. Ex-

cept for image acquisition, we developed these techniques with the intent of overcoming the problems the RV poses.

Tagged MRI acquisition

To obtain within-wall, quantitative motion, we need to mark the tissue at one time point and follow that marker through time. As we mentioned earlier, the MRI tissue-tagging technique provides a noninvasive method for heart-wall motion tracking. The tissue is marked using

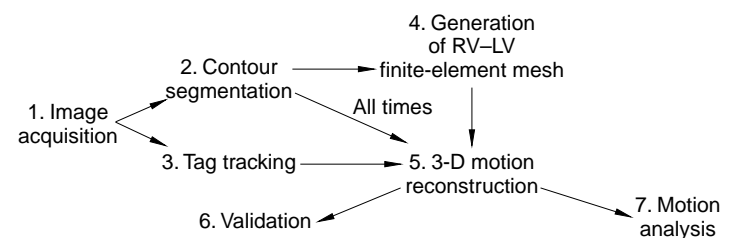


Figure 1. Our flowchart shows the techniques we developed or expanded and the flow of information between those methods: (1) Acquire multiple tagged images from several views to get 3D motion information (over several phases of systolic contractions). (2) Trace contours of the inner and outer ventricular walls from the images. (3) Follow the motion of the tags through successive 2D image frames (what we call image times). (4) Generate the static RV-LV model directly from the contours taken from the initial time. (5) Use the tag and contour information to recover the ventricles' 3D motion. (6) Assess the motion reconstruction method's accuracy and validity. (7) Use mechanical engineering techniques to analyze the recovered motion.

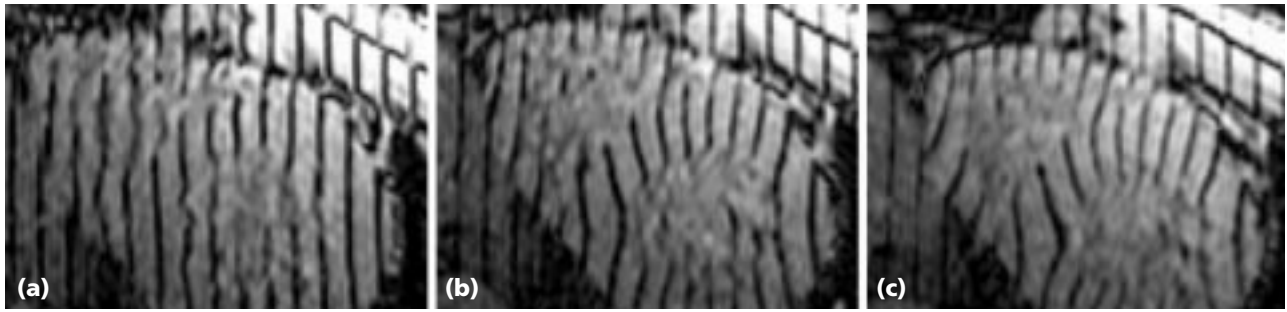
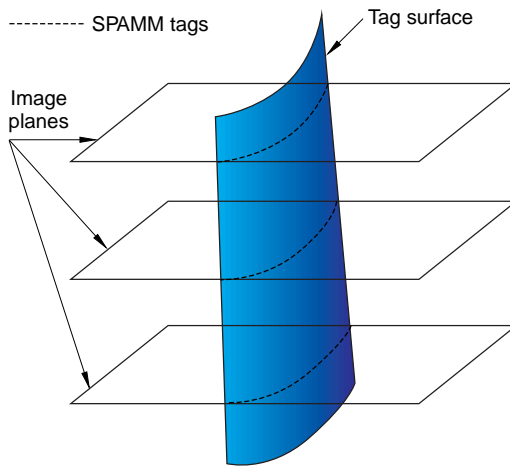


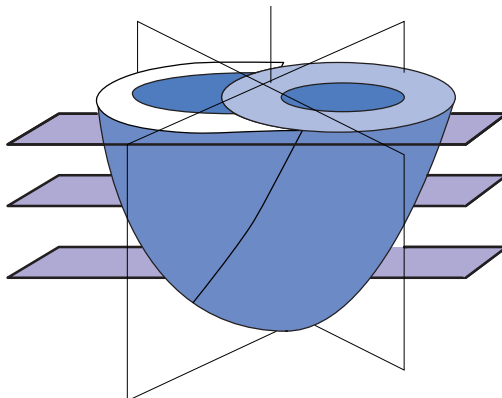
Figure 2. Mid-ventricular short-access one-dimensional tagged MRI images at (a) beginning systole, (b) mid-systole, and (c) end systole.

Figure 3. MRI-SPAMM tagging (SPAtial Modulation of Magnetization—SPAMM is a tissue-tagging technique). The intersection of each tag surface with the image planes produces dark bands or stripes in the images.



much of the same physics as in regular MRI. Prior to imaging, the MRI scanner generates a sequence of nonselective radio frequency excitation pulses, separated by intervals of magnetic-field gradients in the direction perpendicular to the desired tag planes. This causes suppression of the signal from the muscle tissue at finite intervals and effectively marks the tissue in evenly spaced, parallel tag planes.

Figure 4. A schematic biventricular unit with representative image planes. Short-axis image planes run parallel while long-axis image planes are rotated about the LV long axis.



The tagging planes are oriented perpendicular to the image planes so that the signal voids result in corresponding dark stripes in the images (Figure 2). As the originally planar tags deform into curved surfaces, they reveal the tissue motion in a direction normal to their initial configuration. Several adjacent image planes having the same orientation can provide a discrete sampling of the tagged tissue surfaces (Figure 3). As the ventricles move through a particular image plane, different portions of the same tag surface intersect the image plane.

To view tag planes, we use multiple image planes—standard short- and long-axis image views—defined as follows (Figure 4): first, we calculate the LV's long axis, then we define this axis to be the normal to the transverse (or short-axis) image planes, and then we define long-axis image planes perpendicular to the short-axis image planes. We use image planes perpendicular to tag planes to view the tag planes. Each orientation of an image plane is called a *view*, because we view the short axis in the short-axis image planes. Rotating long-axis image planes prevents extremely oblique cuts along the heart walls.

[insert figure 4]

Our method uses two sets of stacked short-axis image planes with tag planes that appear as vertical stripes and a set of rotating long-axis images with tag planes appearing as horizontal stripes. Because each tag plane only provides information about motion in the direction perpendicular to its initial orientation, we must combine three mutually perpendicular tag plane orientations to capture 3D motion information. The schematic in Figure 5 shows these combinations along with the motion information that each combination provides. We used a slice thickness of 6 mm with an 8-mm spacing between short-axis image planes and 20 degrees between long-axis image planes. The scan time we used was approximately 40 minutes.

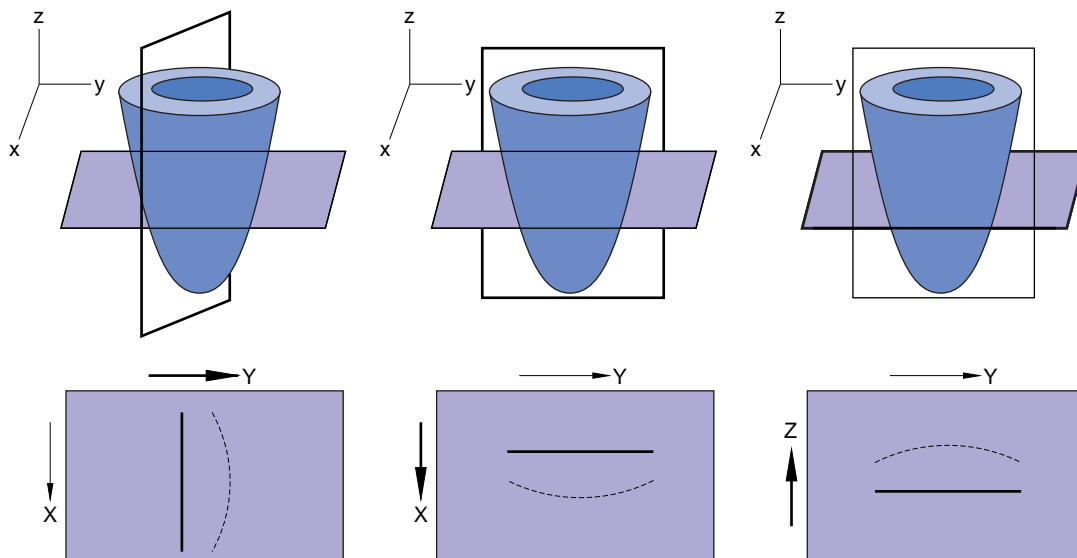


Figure 5. The top row shows the schematic of the LV with image (light) and tag (dark) planes. The bottom row shows 2D images with examples of tag motion from initial (dark lines) to final (dashed lines) times. Highlighted arrows indicate for which direction in the coordination system the shown motion information is provided.

Tag tracking

We followed the tags semiautomatically in successive images using a separate program in the University of Pennsylvania's Department of Radiology (SPAMMVU).⁶ SPATial Modulation of Magnetization (SPAMM) is a tissue-tagging technique Leon Axel developed, and SPAMMVU is SPAMM's visualization utility. The tag extraction method uses a mesh consisting of two sets of mutually orthogo-

nal active contours, or snakes.^{7,8} The snakes are attracted to the voids in the image, and the user can push them away from any local minima with the mouse. We extracted tags with an adaptation of the 2D mesh tool where one orientation of snakes tracks the stripes while the other maintains structural support. Figure 6 shows the initial and final positions of the snakes' tracking orientation from a mesh we used to track 1D tags.

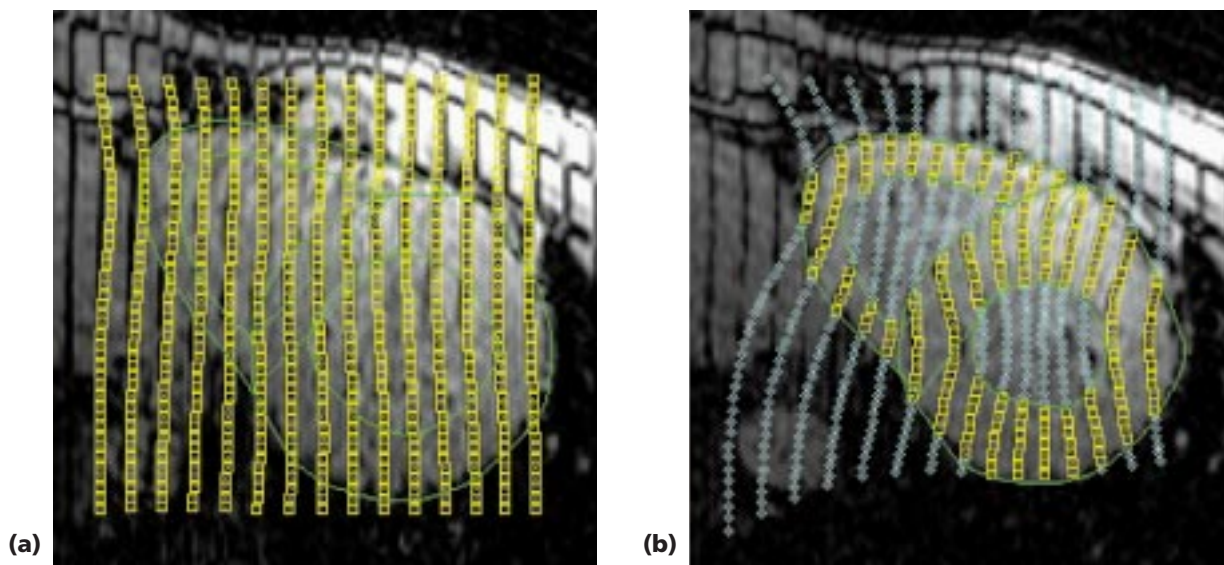


Figure 6. The stripes are tracked by deforming a mesh of interlocked snakes (active contours): (a) the initial mesh at end diastole and (b) the final mesh at the end of the contraction. Lighter-colored squares are marked active because they fall within the contours. The stripes are tracked by deforming a mesh of interlocked snakes.

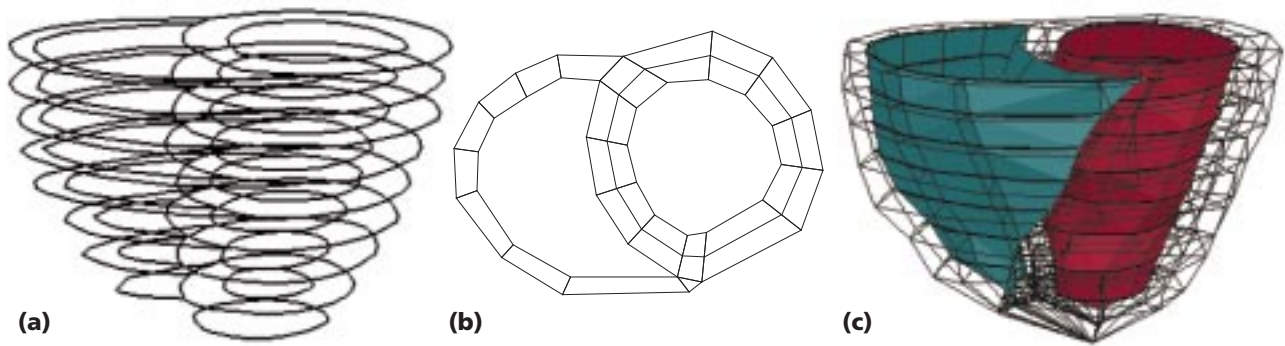


Figure 7. Finite-element mesh geometry: (a) short-axis contours from stacked sets of MR images, (b) a cross-sectional layout of elements, and (c) the final mesh, with shaded endocardial walls of LV (dark pink) and RV (green blue).

Model geometry

Although we can't approximate the RV by any simple geometric primitive, we need an accurate geometric model to reconstruct the 3D motion. Instead of the more commonly used approach of fitting a predefined model to contour data, our approach is to generate a volumetric finite-element mesh directly from contours extracted from end-diastolic images. The heartbeat can be divided into systole (the contraction phase) and diastole (the relaxation phase). Therefore, end diastole is right before the heart contracts and end-systole is at the end of contraction. This automated approach is more flexible and applicable to the complex geometry we're modeling, particularly for disease states that might alter the ventricular geometry in ways that a predefined model might not approximate very well. The finite-element approach results in a piecewise definition of the ventricular geometry—the number and type of element is altered according to the local geometry. The use of existing finite-element mesh generation packages does not provide this control and sometimes requires additional pre- and postprocessing. With our approach, the geometry-building and fitting phases are integrated into one program. We define the finite-element mesh geometry in two stages: we *partition* the contours into the set of model points (nodes) to set up the topology, then we *generate* the finite elements that connect these nodes.

Our algorithm calls for tessellating (or "tiling") the 2D cross-sectional geometry and generating volumetric elements to connect those sections. Because the cross-sectional topology in the main portion of the biventricular unit remains more or less constant in short-axis rather than long-axis views, we used short-axis contours for the mesh generation. Figure 7a shows the stacked set of short-axis contours, which must

be sampled in such a way that elements of the RV and LV are continuous at the insertion points. The contours are divided (points are sampled) equally, but the RV and LV elements need to be continuous at the insertion points. We found the connection with the appropriate outer wall by intersecting the local normal with the epicardial contours. (Endocardial is inner and epicardial is outer.) As shown in Figure 7b, the elements are arranged in two concentric layers in the LV free wall and septum and one layer thick in the RV.

Biventricular geometry is very complex, so we built a discretized volumetric model using finite elements. A finite element's geometry is defined by the location of its vertices (or nodes) and shape functions, which determine the position (and the value of other parameters) of points within the element. (See the "Finite-element shape functions" sidebar for more information.) Given the RV shape's complexity, we used a large number of smaller elements with linear shape functions, rather than larger elements with higher-order shape functions. The finite-element nodes are points from the sampled contours described earlier. To visualize the endocardial and epicardial surface of both the ventricles, we labeled the faces of the finite elements that lie on these surfaces during this mesh-building step and later triangulated them for shaded surface display. The finite elements play a role in both the fitting method and the strain calculation. The total number of elements varies with heart size and a desired number of intervals used in partitioning the contours. We can adjust the number of intervals to provide a desired number of elements and number of model degrees of freedom. The final finite-element mesh (Figure 7c) has 222 elements and 336 nodes.

Finite-element shape functions

Shape functions interpolate a motion variable (displacement, position) from the nodes to a point within the element. For displacement, we can write this as

$$x = \sum_{j=1}^n N_j(e,n,s)x_j,$$

where (x_j, y_j, z_j) is the position of the j th node. The shape functions, N_j , weight the global coordinate of a node according to where a point lies in the local (e,n,s) coordinate system of an element.

Figure B shows the eight-noded and six-noded elements used in the finite-element mesh.¹ The shape functions for an eight-noded parallelepiped are

$$N_1 = (1+x)(1+h)(1+z)$$

$$N_2 = (1+x)(1+h)(1-z)$$

$$N_3 = (1-x)(1+h)(1-z)$$

$$N_4 = (1-x)(1+h)(1+z)$$

$$N_5 = (1+x)(1-h)(1+z)$$

$$N_6 = (1+x)(1-h)(1-z)$$

$$N_7 = (1-x)(1-h)(1-z)$$

$$N_8 = (1-x)(1-h)(1+z)$$

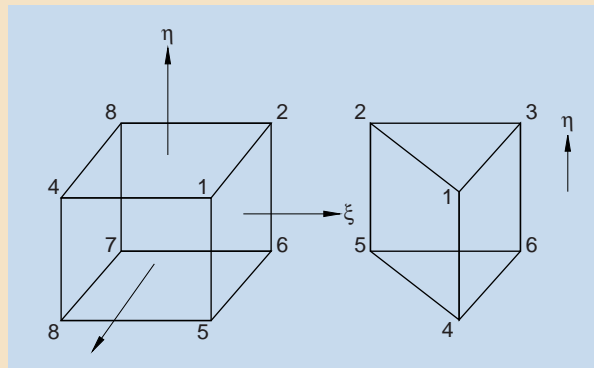


Figure B. Elements used to build deformable models, including the local coordinate system and numbered nodes: (a) eight-node parallelepiped and (b) six-node wedge.

Reference

1. O.C. Zienkiewicz and R.L. Taylor, *The Finite Element Method*, 4th ed., McGraw-Hill, New York, 1989.

3D motion reconstruction

Once we've generated an accurate geometric model of the ventricles, we use information from image-derived data to capture the full 3D motion of the ventricles. As we mentioned earlier, the deformable modeling approach is a commonly used method in which a model deforms to fit to data using energy minimization or a classical physics-based equation of motion.⁹ The specifics of how to deform the model and apply the deformation constraints vary with the particular application. Previous work in our laboratory¹⁰ has successfully used Lagrange's equations of motion with spring-like (proportional to displacement) forces that attract the model to image-derived data. Although we maintain that basic framework in this work, application of the fitting technique to the RV has led to a major alteration in the force calculation and the use of local, rather than global, smoothing.

Model dynamics

We recovered the 3D motion by fitting the geometric model to image-derived data. To recover the motion through systole, we fit model sequentially to data from each image time phase.

For fitting within each phase, model deformation follows a reduced form of Lagrange's equation of motion:

$$\mathbf{q} + \mathbf{K}\mathbf{q} = \mathbf{f}_q$$

where the vector \mathbf{q} contains the displacement degrees of freedom and the vector \mathbf{f}_q contains the image-derived forces. The inertial term is neglected, and we use the viscous damping (with a coefficient of 1) to let the model come to rest when it reaches the position most consistent with the data. Due to the relative sparsity of the data available from the tagged images, localized spatial smoothing is also added through the finite-element stiffness matrix, \mathbf{K} . We can also view stiffness as an internal resistance that results in a force equal to $\mathbf{K}\mathbf{q}$. Using these considerations, Lagrange's equation of motion is written for each node i as

$$\mathbf{q}_i = \mathbf{f}_{i,internal} + \mathbf{f}_{i,external}$$

where \mathbf{q}_i is the 3D nodal displacement, $\mathbf{f}_{i,internal} = [\mathbf{K}\mathbf{q}]_i$ is an internal stiffness force, and $\mathbf{f}_{i,external}$ is an external, image-derived force. We only use these forces to deform our model—they are not meant to replicate the actual forces or material properties of cardiac tissue.

There are two types of external image-derived forces: contour forces and SPAMM (\mathbf{f}_{SPAMM})

forces. The contour forces are derived from the traced contour data. All external forces are directly proportional to the distance between the model and image-derived data: $\mathbf{f}_{data} = \mathbf{d}_{data}$, where \mathbf{d}_{data} is the distance from a point on the model to the location of the appropriate data. We can view them as forces arising from springs attached between points on the model and the data, where the spring coefficient is set to 1. We focus here on the external SPAMM force derived from the tag data.

External forces from SPAMM data

The SPAMM markers provide information about motion within the myocardium (the heart muscle). We refer to these markers in general as *tag surfaces* and to the initially planar tags as *tag planes*. The SPAMM force calculation is based on the fact that the tag data provide information about the time evolution of the deformation of markers in the actual heart muscle. Because the initial position of both the model and the tags are known, we can hook the simulated tag planes that coincide with the initial tag plane positions onto the model. Because these planes are registered to the deformable model, we call them *material surfaces*. The material surfaces are modeled as a triangulated set of points, and the SPAMM forces are then calculated between these points and tag data from the images. The forces are then distributed to the finite-element nodes—now the model is pulled toward this data. By simultaneously fitting the deformable model to tag data

provided in three mutually perpendicular directions, we can reconstruct the 3D motion.

Although we have a 3D motion model, the original tag data exists only at the original image planes. Additionally, we encountered a problem during our method development: if we only registered points located in the image planes, the movement of these registered points out of the image plane due to through-plane motion meant that we were calculating subsequent motion information in a plane where the initially registered tagged material no longer resided. Because the RV can move through more than two short-axis image planes (about 15 mm near the ventricle's base), it affected result accuracy. We overcame this limitation by noting that the tag lines seen in the MRI images are the intersections of the tag surfaces with the image planes (Figure 3). If the image plane separation is small enough (about 8 mm in our case), there will be only a small variation in the shape of the tag surface between each image plane. Therefore, we can reconstruct the position of the entire tag surface from the tag stripe positions at each image time phase. The reconstruction results in the availability of tag data irrespective of the image plane locations. Figure 8 shows tag surfaces along with their original stripes.

The SPAMM forces are designed to pull the model material surfaces toward the reconstructed tag surfaces as shown in Figure 9. Thus, a force is calculated between each material point, mp , and the appropriate reconstructed tag surface. The force direction is determined by keeping in mind that, as the tagging planes deform into surfaces, they only provide motion information normal to their original orientation. We also track the SPAMM error, \mathcal{E}_{SPAMM} , which is the RMS (root mean square) average of the distance equivalent forces, \mathbf{f}_i , from all material points defining sets of material surfaces in all three orientations.

Internal forces due to stiffness

Our model's degrees of freedom are the 3D displacements of the finite-element nodes. Forces

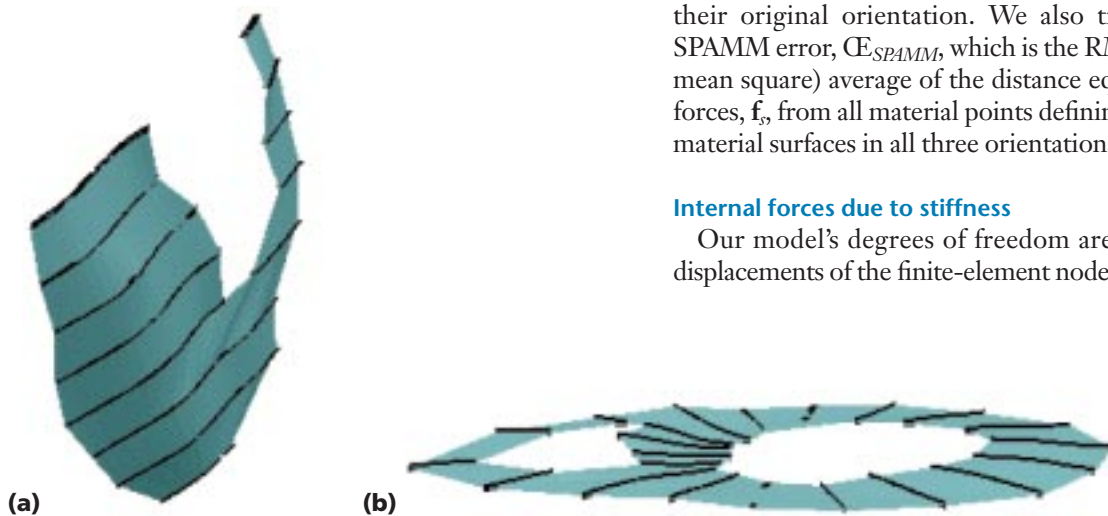


Figure 8. Reconstructed tag surfaces (shown shaded) along with original tag stripes (black lines): (a) stripes originating from stacked, short-axis image planes, and (b) stripes originating from a set of rotating long-axis image planes.

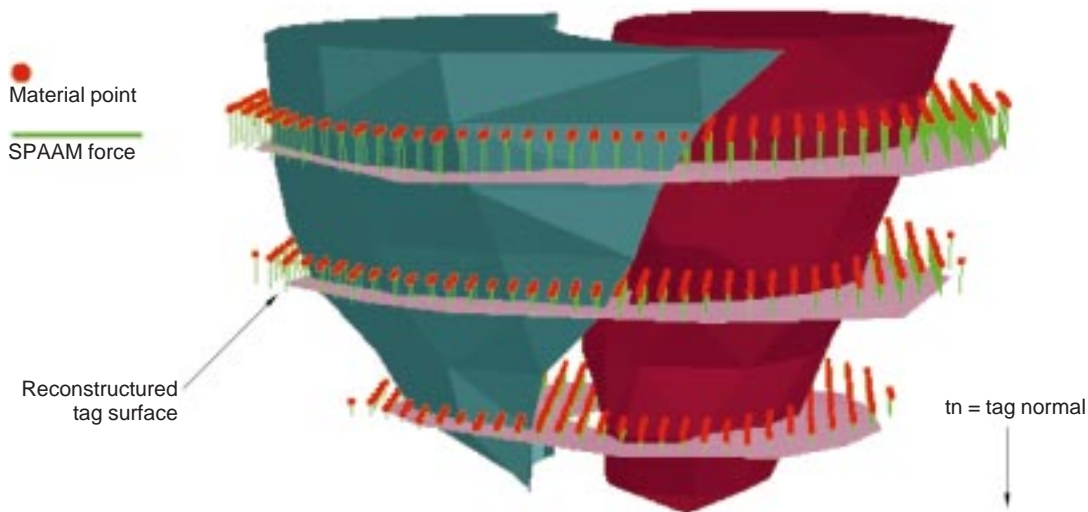


Figure 9. Each collection of material points defining a material surface (not drawn) is attracted to the corresponding tag surface via the SPAMM forces. This figure shows several tag surfaces reconstructed from the long-axis view along with model endocardial walls.

calculated from segmented contours and tags might have inaccuracies in the data due to human error during segmentation or image noise. To account for the discrete sampling of motion data due to the tags and factors that cause inaccuracies in the input data, a stiffness component adds smoothing to the deformable model. In our formulation, stiffness is considered an internal force, $\mathbf{f}_{i,internal}$. To impose a continuity and smoothing constraint between image time phases, each element is considered to consist of isotropic, linear, compressible material.

The element force vector, \mathbf{f}_e , contains the forces on the element nodes. It is calculated for each element as

$$\mathbf{f}_e = \mathbf{K}\mathbf{d}_e$$

where \mathbf{d}_e contains the nodal displacements. The finite-element stiffness matrix \mathbf{K} incorporates the element's geometry and material properties. (A different text contains a detailed derivation of the finite-element formulation for calculating the stiffness matrix \mathbf{K} .¹¹) To prevent element distortions of the linear elements, we recalculate the stiffness matrix after fitting to each time phase, thereby making the smoothing piecewise linear. Each element force \mathbf{f}_e contributes to the forces at the nodes of the element $\mathbf{f}_{i,internal}$.

Kinematic analysis

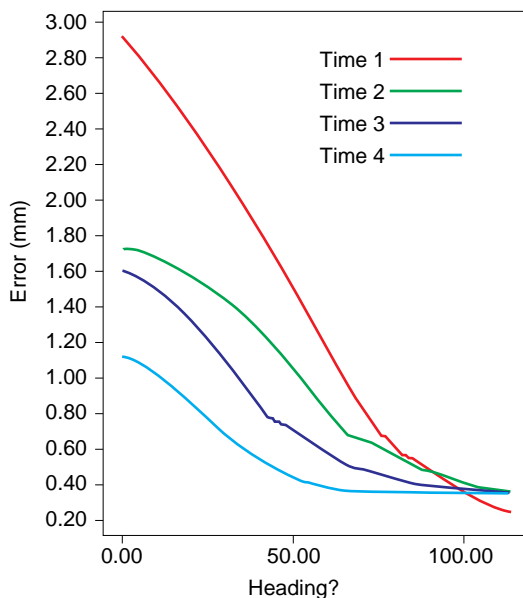
The 3D motion reconstruction provides the

ventricular model's estimated nodal displacements. However, because simply viewing a finite-element mesh's motion is of little use to researchers and clinicians, an important area of research is being able to quantify the motion and visualize the results efficiently. Previous LV studies¹⁰ described the reconstructed motion in terms of variables that clinicians are already familiar with for that ventricle—for example, twisting and radial contraction. In a preliminary work for the current motion-fitting method, we attempted to quantify twisting in the RV.¹² However, due to the ventricle's complex shape, it was difficult to find a single axis about which to calculate twisting and radial contraction. Even when an axis was specified, these circular measures were not satisfactory for the crescent-shaped RV.

Instead, we use a measurement that is coordinate-system independent. We use the initial, end-diastolic position as a point of reference for our measurements. The displacement of individual points is an indicator of motion, whereas principal strains¹³ provide a deformation measurement. Because the heart muscle's contraction is almost directly related to the degree of deformation, we focus our analysis on analyzing strain.

Strain can be the ratio of the change in length of an arbitrary line segment in the material to its initial length. When looking at strain surrounding a particular point in a 3D volume, we must specify the line segment's orientation. Therefore, we use tensors to define the strain magnitude, direction, and orientation as follows.

Figure 10. Convergence behavior of the fitting technique for a representative study. Decrease in $\mathbb{C}_{S_{PAMM}}$ versus iteration step t for all four image time phases.



Given the initial and final positions of a point in the $\mathbb{C}_{S_{PAMM}}$ ∂x_p^i X and x , respectively, we first calculate $F_{pq} = \frac{\partial x_p^i}{\partial X_q}$ deformation gradient tensor F :

where the subscripts p and q range from 1 to 3 and denote one of the 3D Cartesian coordinates. The tensor F includes both the rotation and deformation around a point in the material. The Lagrangian strain tensor, E , only includes the

deformation of the material with respect to its initial configuration, and is related to F as follows $\mathbb{E} = \frac{1}{2}(F^T F - I)$

where I is the identity matrix. The Lagrangian strain formulation describes systolic deformation in a region surrounding a point in the heart relative to its initial position at end diastole.

Because the Lagrangian strain is a tensor, which includes orientation information, it is still defined relative to a reference coordinate frame. At any point in the material, there will be a direction for which the strain is the greatest or smallest. The eigenvectors of E are these principal directions. The largest ($E1$) and smallest ($E3$) of the eigenvalues are the maximum and minimum principal strains. A positive value indicates extension while a negative value indicates compression.¹³ Because the principal strains are scalars, we are now free of any reference coordinate system.

Results

We applied the 3D motion reconstruction technique to synthetic data and data from nine human subjects, with the same smoothing parameters for all cases. During the fitting, the RMS error between the material surfaces and reconstructed tag data $\mathbb{C}_{S_{PAMM}}$ is calculated. The convergence behavior was similar for all data sets. Figure 10 shows the convergence of $\mathbb{C}_{S_{PAMM}}$ for all image time phases from normal data. Considering the system's convergence behavior, we terminated the fitting for data from a certain image time phase when the changes in $\mathbb{C}_{S_{PAMM}}$ and $\mathbb{C}_{contour}$ were both less than 2%. The total fitting time for the experiments was about 40 minutes (8 minutes for the synthetic data) on an SGI 02 RS10000 workstation. Because several algorithms have not yet been optimized, we estimate that we can reduce the fitting time by a third. The time for the automatic mesh generation was relatively small, about 15 seconds.

We used two forms of validation—synthetic data and comparing the model to the original images. For the first form, we generated synthetic data for a known deformation and geometry. We fed the synthetic data into the motion reconstruction program, and we compared the resulting displacement with the known displacement. The displacement errors calculated at the nodes were < 0.6 mm RMS, which is less than the resolution of the images (about 1 mm), and 2% of the original displacements. For the second form of validation, we compared the results

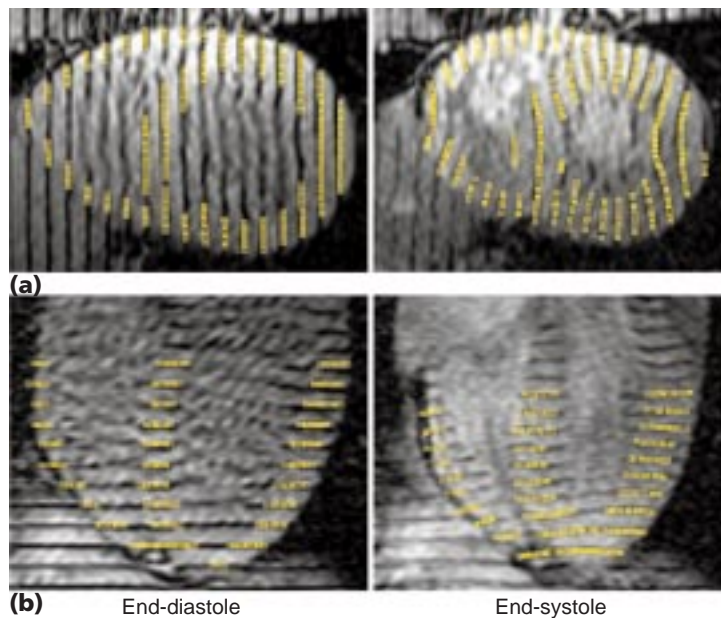


Figure 11. The intersections of model material surfaces with the image plane locations shown along with the original end-diastolic and end-systolic images: along the (a) short axis and (b) long axis.

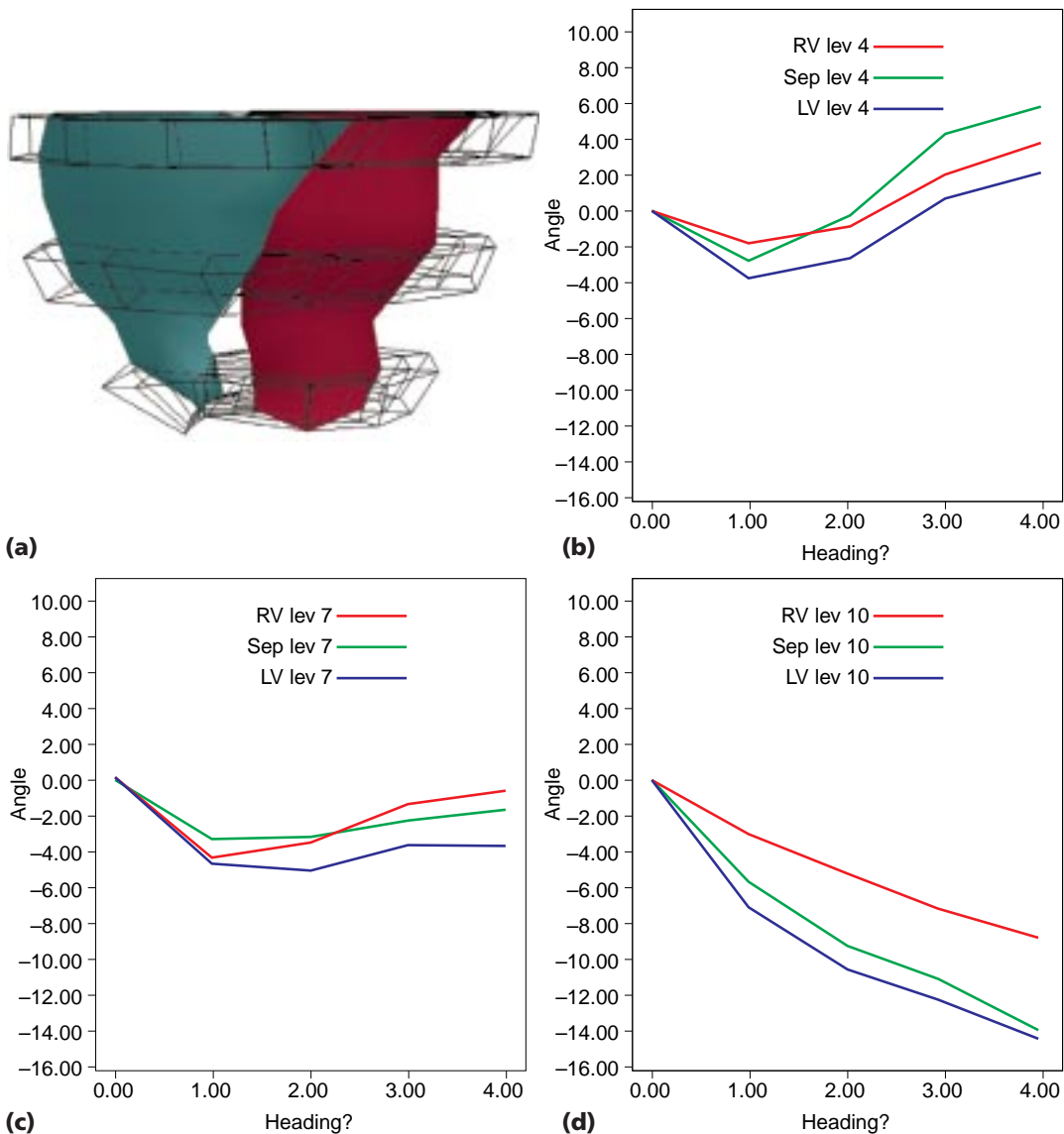


Figure 12. Motion about the LV long axis at several levels, or slices, in the model: (a) slices relative to endocardial walls (shown shaded). The graphs show angular positions as a function of image time phase for (b) basal, (c) mid, and (d) apical slices. Positive angles are counterclockwise.

of the 3D motion reconstruction to the original images from which we derived the data. For each view, we show the end-diastolic and end-systolic images with an overlay of the model material plane–image plane intersections in Figure 11. The figure shows agreement, although it appears that the model was too stiff in some areas to fit the entire curvature of the tags. These observations can help in future model improvements.

All five normals exhibited similar qualitative and quantitative behavior. Figure 12 shows the motion of points in the RV and LV for several element slices—the angular displacements about the LV long-axis are plotted for each wall at each

level. Within each level, the angular displacement is similar for the RV free wall, LV free wall, and septum. When comparing basal, mid-ventricular, and apical levels, notice that all regions initially rotate clockwise. The basal slice subsequently changes direction and rotates in a counterclockwise direction while the apex continues to rotate clockwise.

Figure 13 shows the model's motion (looking at the free wall) over all time phases for a typical normal study. The path of points in the center of the RV free wall is plotted along with a color plot of point displacement on the endocardial wall. The paths of most points in the free

wall are anterior and toward the apex. The color plot of displacement in the figure reveals a nonuniform distribution. The greatest amount of displacement in the biventricular unit occurs

in the RV's basal free wall. We used linear regression to assess the presence of decreased base–apex displacement in the RV free wall ($R = .724$). (R is the regression coefficient.)

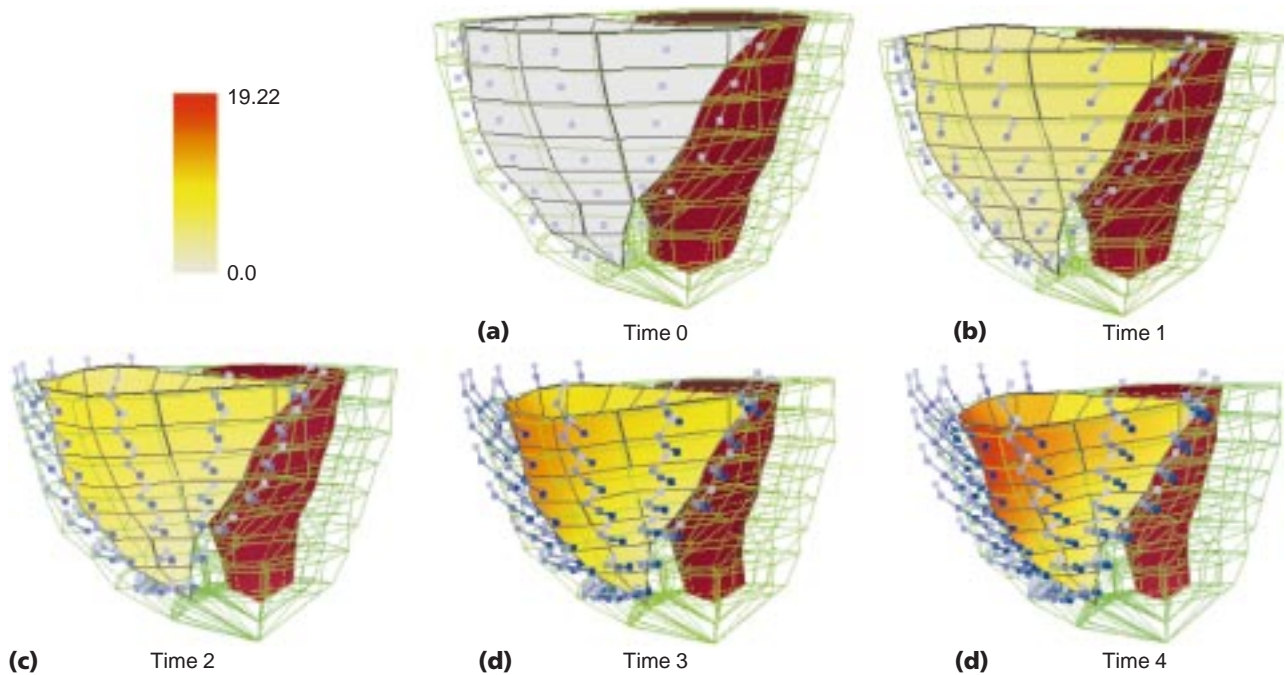


Figure 13. Normal heart displacement through systole shown as a color plot on the RV endocardial free wall. The paths of points located in the centers of the elements are shown from end diastole (white) to end systole (blue).

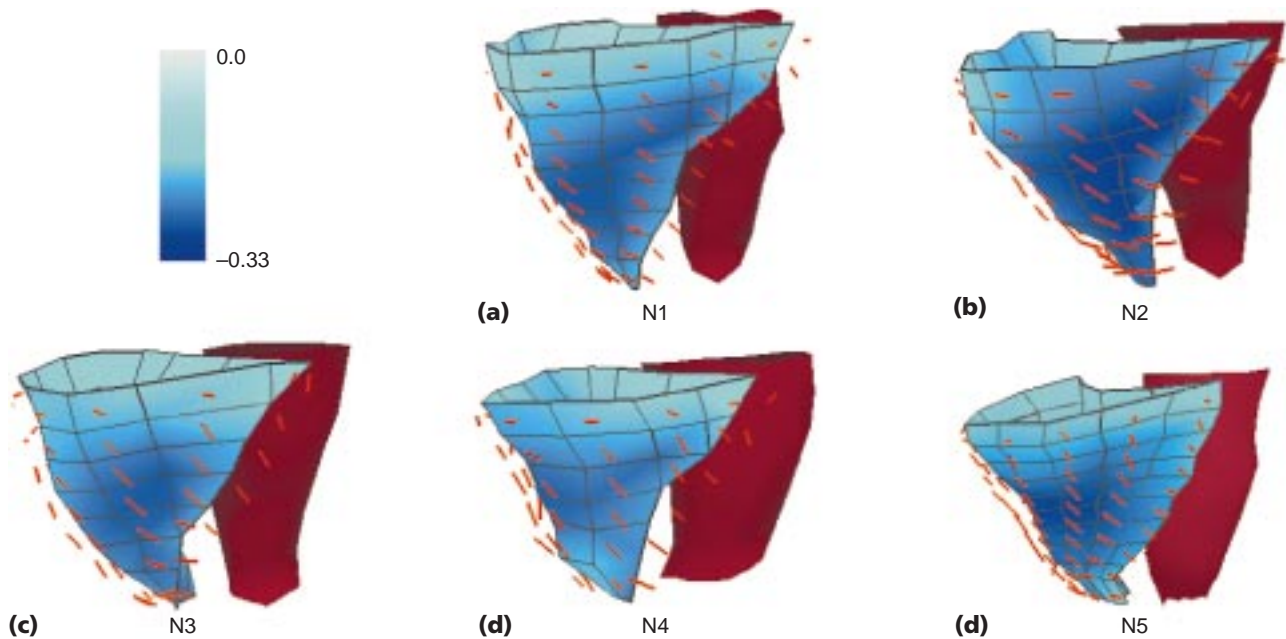


Figure 14. Normal E3: recovered end-systolic position of all normal studies. A color plot of minimum principal strains is on the RV endocardial free wall. Red lines are the minimum principal strain directions drawn at the centers of the elements, with lengths normalized by the strain magnitude.

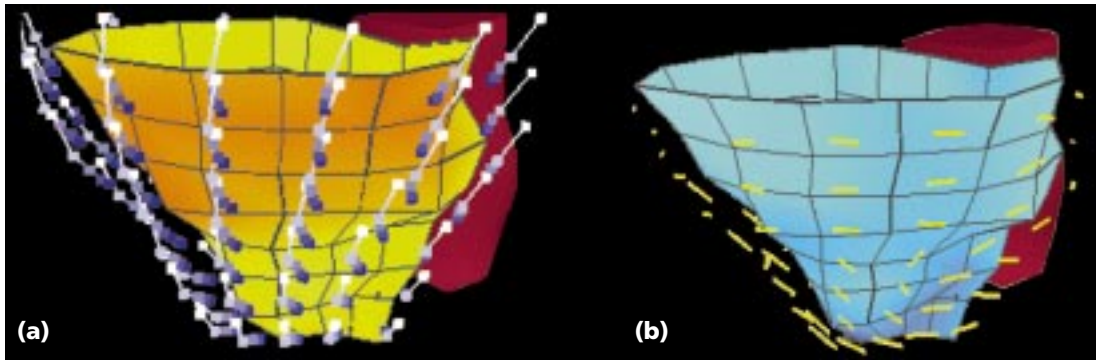


Figure 15. Motion reconstruction of RV hypertrophy. The RV is shown at end systole with color plots on the endocardial walls. Color scales are the same as in normals: (a) displacement along with the paths of points located in the centers of the elements from end diastole (white) to end systole (blue), and (b) strain map of minimum principal strain. Dark lines are the minimum principal strain directions.

Regional deformation

To quantify the magnitude of the greatest muscle contraction between end diastole and end systole, we calculated the minimum principal strain (E_3). Figure 14 shows a color plot on the endocardial surface of the RV free wall of E_3 at end systole for all five normal subjects. The associated principal directions are plotted at the mid-ventricular, with lengths normalized according to the maximum contraction at those locations. We can see a decreasing trend in the base-to-apex contraction. Basal E_3 was significantly smaller than in other regions (probability $< .002$). This suggests that mid- and apical portions of the heart have the greatest contraction to pull the base of the heart toward the apex.

RV hypertrophy

A common reaction of the RV to increased pressures or blood volume is to increase its mass, a

process called hypertrophy. Increased pressures are usually a result of some sort of blockage in the lung (such as an embolism). Volume overload is usually a result of overcirculation due to congenital heart disease.¹ Both types of hypertrophy can alter cellular contractile function,¹⁴ produce prolonged action potentials,¹⁵ and result in a lowered ejection fraction.¹ Furthermore, increased pressures in the RV cavity can cause the septum to bulge into the LV cavity, thereby decreasing LV ejection fraction.¹⁶ The changes in the actual pumping mechanisms in the hypertrophied heart are not well-characterized.

Figure 15a shows the paths of points in the RV free wall along with a color plot of the displacement for a representative RV hypertrophy (RVH) study. The paths of the points are different from the normals, with no anterior motion of points in the free wall. When compared to normals, we

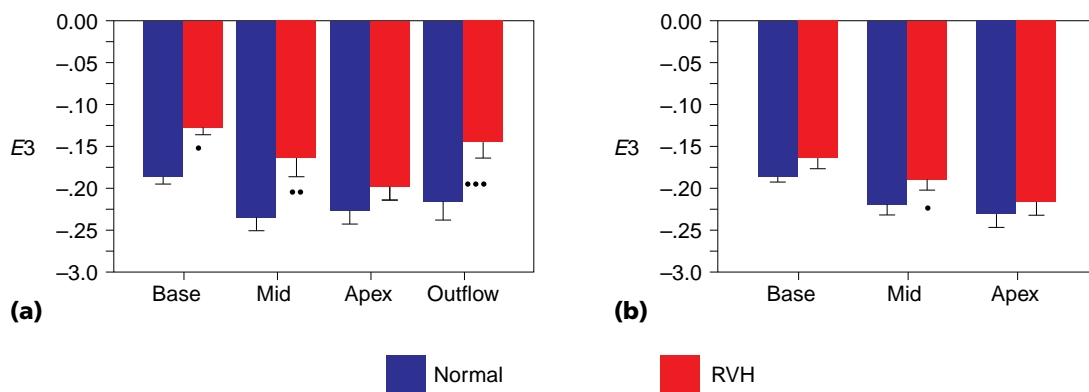


Figure 16. A comparison between regions of the strain in normals versus RVH patients: (a) In the freewall, all regions had an average decrease in $|E_3|$, with significant differences in the base ($p < .0001$), mid-ventricle ($p < .002$), and outflow tract ($p < .002$). (b) In the septum, all regions had an average decrease in $|E_3|$, with significant differences in the mid-ventricle ($*p < .008$). We adjusted significance levels from .05 by the number of regions within each wall. Values are mean \pm standard deviation.

found that average displacement decreased in most regions of the free wall and septum for RVH patients ($p < .01$). The strains also decreased (Figure 15b)—note that the color scale is the same as that for the normals. Regional differences are better seen in the bar plot in Figure 16. The average value of $|E3|$ decreased for all regions in both the free wall and septum during RVH and was significantly different in most regions. The angles of the minimum principal strain directions are more horizontal for the RVH case compared to the normals. Although we couldn't find statistically significant changes for the current number of subjects, this difference indicates that the direction of maximal contraction has actually altered. Although others have observed changes in muscle cell orientation during hypertrophy, the consequences of these changes have not been measured until now.

The MRI tissue-tagging technique gives researchers the first glimpse into how the heart actually beats. We designed our technique to accommodate for the RV's thinness and complex geometry—it provides both regional and distributed global information about RV strain and displacement. An example of the usefulness of this method is the observation that although the maximum displacement occurs at the RV base, the maximum contraction is in the mid-region and apex, which we could not have observed without a quantitative analysis of tagged tissue. This method opens the way for characterizing normal RV wall motion, as well as for deriving global motion parameters that are more intuitive to physicians, akin to those found for the LV. Once the normal RV motion is characterized on a global and regional scale, researchers can apply our technique to abnormal cases to determine which motion variables are the best indicators of various diseases.

References

1. D. Barnard and J.S. Alpert, "Right Ventricular Function in Health and Disease," *Current Problems in Cardiology*, Vol. 12, No. 7, July 1987, pp. 422–429.
2. L.M. Boxt, "Radiology of the Right Ventricle," *Radiological Clinics of North America*, Vol. 37, No. 2, 1999, pp. 379–400.
3. L. Axel and L. Dougherty, "Heart Wall Motion: Improved Method of Spatial Modulation of Magnetization for MR Imaging," *Radiology*, Vol. 172, No. 2, Aug. 1989, pp. 349–350.
4. W.G. O'Dell et al., "Three-Dimensional Myocardial Deformations: Calculation with Displacement Field Fitting to Tagged MR Images," *Radiology*, Vol. 195, No. 3, June 1995, pp. 829–835.
5. A.A. Young, Z.A. Fayad, and L. Axel, "Right Ventricular Mid-Wall

Surface Motion and Deformation Using Magnetic Resonance Tagging," *J. Applied Physiology*, Vol. 271, No. 6, Dec. 1996, pp. 2677–2688.

6. L. Axel et al., "SPAMMVU: A Program for the Analysis of Dynamic Tagged MRI," *Proc. Soc. Magnetic Resonance in Medicine 12th Ann. Meeting*, ISMRM, 1993, p. 724.
7. M. Kass, A. Witkins, and D. Terzopoulos, "Snakes: Active Contour Models," *Int'l J. Computer Vision*, Vol. 1, No. 4, Mar. 1987, pp. 321–331.
8. A.A. Young et al., "Tracking and Finite Element Analysis of Stripe Deformation in Magnetic Resonance Tagging," *IEEE Trans. on Medical Imaging*, Vol. 14, No. 3, Sept. 1995, pp. 413–421.
9. T. McInerney and D. Terzopoulos, "Deformable Models in Medical Image Analysis: A Survey," *Medical Image Analysis*, Vol. 1, No. 2, Winter 1996, pp. 91–108.
10. J. Park, D. Metaxas, and L. Axel, "Analysis of Left Ventricular Wall Motion Based on Volumetric Deformable Models and MRI-SPAMM," *Medical Image Analysis*, Vol. 1, No. 1, Winter 1996, pp. 53–71.
11. O.C. Zienkiewicz and R.L. Taylor, *The Finite Element Method*, 4th ed., McGraw-Hill, New York, 1989.
12. E. Haber, D.N. Metaxas, and L. Axel, "Motion Analysis of the Right Ventricle from MRI Images," *Medical Image Computing and Computer-Assisted Intervention*, Springer-Verlag, New York, 1998, pp. 177–188.
13. A.J.M. Spencer, *Continuum Mechanics*, Longman, London, 1980.
14. H. Tsutsui, "Role of Microtubules in Contractile Dysfunction of Hypertrophied Cardiocytes," *Circulation*, Vol. 90, No. 1, July 1994, pp. 533–555.
15. C. Chouabe, "Reduction of I(Ca,L) and I(tol) Density in Hypertrophied Right Ventricular Cells by Simulated High Altitude in Adult Rats," *J. Molecular and Cellular Cardiology*, Vol. 29, No. 1, Jan. 1997, pp. 193–206.
16. A.V. Noordegraaf, "The Effect of Right Ventricular Hypertrophy on Left Ventricular Ejection Fraction in Pulmonary Emphysema," *Chest*, Vol. 112, No. 3, Sept. 1997, pp. 640–645.

Idith Haber is a researcher at Children's Hospital of Boston and Harvard Medical School. Her interests include image analysis, mechanical analysis of heart motion, and congenital heart disease. She received her PhD in bioengineering from the University of Pennsylvania. Contact her at the Dept. of Bioengineering, Univ. of Pennsylvania, Philadelphia, PA 19104-6389.

Dimitris N. Metaxas is an associate professor of computer science at the University of Pennsylvania. His technical interests include computer vision and deformable modeling. He received his PhD in computer science from the University of Toronto. Contact him at the Computer and Information Science Dept., Univ. of Pennsylvania, Philadelphia, PA 19104-6389.

Leon Axel is a professor of radiology at the university of Pennsylvania Medical School. His interests include MRI perfusion imaging and image analysis. He received his PhD in physics from Princeton University and his MD from Stanford University. Contact him at the Dept. of Radiology, Univ. of Pennsylvania, Philadelphia, PA 19104-6389.